Supplementary Material

On-chip twisted hollow-core light cages: enhancing planar photonics with 3D nanoprinting

Johannes Bürger[a], **Jisoo Kim**[b,c], **Thomas Weiss**[d,e], **Stefan A. Maier**[f,g], **Markus A. Schmidt**[b,c,h,*]

[a]Chair in Hybrid Nanosystems, Nanoinstitute Munich, Ludwig-Maximilians-Universität Munich, Königinstraße 10, 80539 Munich, Germany
[b]Leibniz Institute of Photonic Technology, Albert-Einstein-Str. 9, 07745 Jena, Germany
[c]Abbe Center of Photonics and Faculty of Physics, Friedrich-Schiller-Universität Jena, Max-Wien-Platz 1, 07743 Jena, Germany
[d]Institute of Physics, University of Graz, Universitätsplatz 5, 8010 Graz, Austria
[e]4th Physics Institute and SCoPE, University of Stuttgart, Pfaffenwaldring 57, 70569 Stuttgart, Germany
[f]School of Physics and Astronomy, Monash University, Clayton, Victoria 3800, Australia
[g]The Blackett Laboratory, Department of Physics, Imperial College London, London SW7 2AZ, United Kingdom
[h]Otto Schott Institute of Materials Research (OSIM), Friedrich-Schiller-Universität Jena, Fraunhoferstr. 6, 07743 Jena, Germany

*Markus A. Schmidt, markus-alexander.schmidt@uni-jena.de

Here, we report additional results and relevant background information on the following topics:

S1 Overview of works on twisted waveguides

Different types of on- and off-axis twisted waveguides are reported in the literature. Tab. S1, shown on the next two pages, presents a broad selection of works in order of achieved (or theoretically analyzed) twist rate. Cross sections of these waveguide geometries are depicted in Fig. S1. A graphical overview of this table is available in Fig. 6.

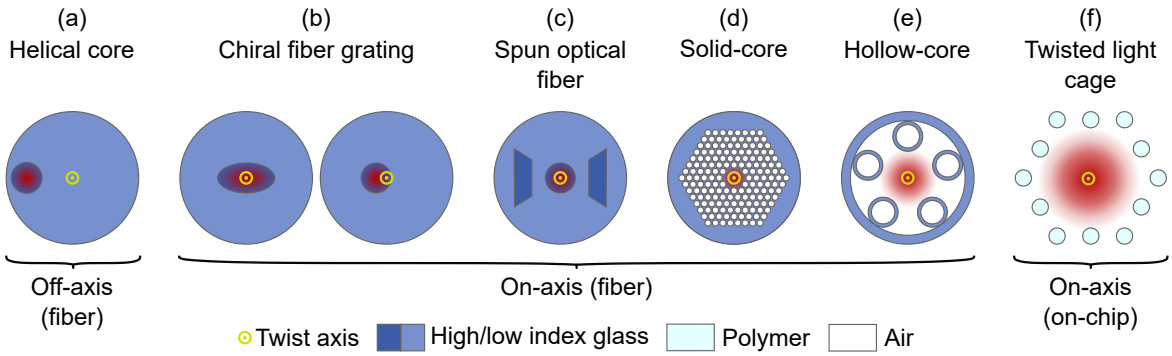

Fig S1 Different on- and off-axis twisted waveguide geometries. The waveguides are twisted along the axial direction (into the plane of the paper) with the location of the twist axis shown in yellow. Twisted waveguides are typically realized from fibers (a-e), while this work investigates 3D-nanoprinted twisted waveguides, allowing on-chip integration (f). Note that chiral fiber gratings either feature an elliptical core or a slightly eccentric circular core (b). Spun optical fibers are often realized from bow-tie fibers (c).

To showcase the potential of 3D nanoprinting, a reference from 2009 on helical metasurfaces by Gansel et al. was included. This work reports the - to our knowledge - smallest pitch distance achieved so far with this technology: 1.8 µm [95]. However, as the total length of these helices

is only about 5 μm, this result is not directly applicable in the context of the twisted waveguides presented in this thesis.

Table S1 Comparison of works on twisted waveguides.

Type	Fabrication method	Twist period P [µm]	Radius ρ [µm]	$\alpha\rho$	Year	Ref.
On-axis twisted waveguides with off-axis rods						
Twisted light cage	3D nanoprinting	90	14[a]	1.00	2024	**This work**
Coreless PCF	3D nanoprinting	200	40[a]	1.26	2020	Bertoncini [40]
Solid-core PCF	Post-processing (CO2 laser)	341	16[a]	0.29	2012	Wong [26]
Solid-core PCF	Post-processing (CO2 laser)	435	16[a]	0.23	2013	Xi [10]
Solid-core PCF	Post-processing	456	16[a]	0.22	2015	Wong [73]
Solid-core PCF	Post-processing (CO2 laser)	622	16[a]	0.16	2013	Xi [37]
Coreless PCF	Preform spinning	2,000	41[a]		2016	Beravat [15]
Solid-core PCF (6 cores)	Preform spinning	2,200	6[b]/18[a]	0.02/0.05	2017	Russell [25]
Solid-core PCF (3 cores)	Preform spinning	2,500	2.5[a]	0.006	2020	Loranger [74]
Coreless PCF	Preform spinning	3,600	41[a]	0.07	2019	Roth [16]
Solid-core PCF (3 cores)	Post-processing (CO2 laser)	5,000	3[b]/16[a]	0.004/0.02	2014	Xi [108]
Solid-core PCF (3 cores)	Preform spinning	5,000	5.2[b]/16[a]	0.007/0.02	2022	Zeng [21]
Hollow-core PCF (single ring)	Preform spinning	11,900	48[a]	0.025	2018	Roth [8]
Hollow-core PCF (single ring)	Preform spinning	12,400	34[a]	0.017	2017	Edavalath [20]
On-axis twisted chiral fiber gratings						
Chiral intermediate period grating	Post-processing (open flame)	24	0		2021	Zou [81]
Chiral intermediate period grating	Post-processing (oven)	45	0		2004	Kopp [7]
Chiral long period grating	Post-processing (oven)	78	0		2004	Kopp [7]
Chiral long period grating	Post-processing (oven)	300	¡1		2005	Ivanov [102]
Chiral long period grating	Post-processing (CO2 laser)	400	¡1		2021	Ren [79]
Chiral long period grating	Post-processing (CO2 laser)	811	0		2004	Oh [103]

Type	Fabrication method	Twist period P [µm]	Radius ρ [µm]	$\alpha\rho$	Year	Ref.
Off-axis twisted waveguides						
Helix metasurface[c]	3D nanoprinting/electroplating	1.8	0.5	1.75	2009	Gansel [95]
Off-axis twisted waveguide	3D nanoprinting	500	40	0.5	2020	Gao [39]
Chiral long period grating	Post-processing (oven)	589	52	0.55	2010	Kopp [104]
Off-axis solid-core PCF	Preform spinning	1,880	95[b]	0.32	2009	Argyros [106]
Helical core fiber	Preform spinning	2,000	184	0.58	1985	Varnham [107]
Chirally-coupled-core fiber	Preform spinning	6,100	27	0.03	2011	Ma [110]
Helical waveguide array	Direct laser writing in glass	10,000	10	0.006	2018	Stutzer [111]
Fiber wound around cylinder	Macroscopic winding	12,000	48,000	25	1984	Ross [112]
Fiber wound around cylinder	Macroscopic winding	300,000	280,000	5.9	1986	Tomita [94]
On-axis spun optical fiber (commercially available)						
Bow-tie (SHB1250(7.3/80)-2.5mm)	Preform spinning	2,500	0			Fibercore [113]
Bow-tie (SHB1250)	Preform spinning	4,800	0			Thorlabs [52]
Polarization maintaining fiber (SH 1310_125-5/250)	Preform spinning	5,000	0			YOFC [109]
Theory & simulation						
Frenet-Serret, helicoidal, and Overfelt waveguide	-	50	14	1.76	2024	Bürger [41]
Frenet-Serret waveguide	-	118[d]	3.5[d]	0.19	2021	Chen [105]
Twisted solid-core PCF	-	622	12[a]	0.12	2013	Weiss [38]

[a] Radius corresponding to outer rod.
[b] Radius corresponding to off-axis core.
[c] Not used as a waveguide because maximal achieved length is only about 5 µm.
[d] For a wavelength of 770 nm.

S2 Multimode versus single-mode strand light cages

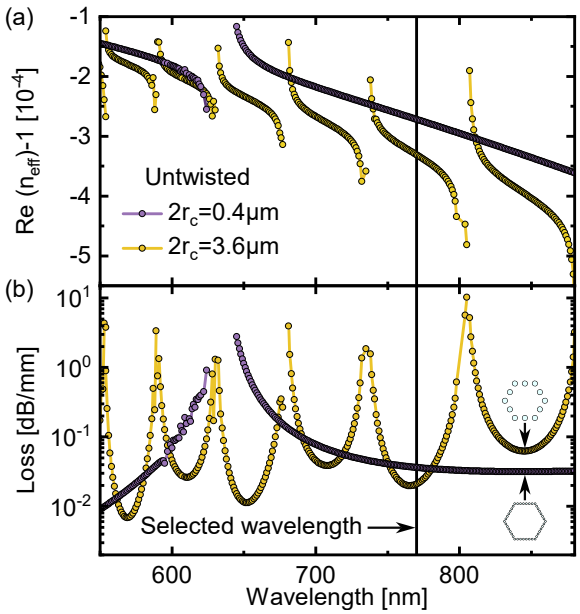

Fig S2 Comparison between multimode and single-mode strand light cages. Spectral distribution of the real part of the effective index (a) and attenuation (b) of the fundamental mode of the untwisted waveguides. The single-mode strand light cage (purple) does not feature any core-strand resonances for wavelengths larger than 650 nm. All simulations in this work that use a fixed wavelength are performed at 770 nm, which is located in a transmission band of the multimode strand light cage (yellow). Insets in (b) depict the geometries. A simplified version of the single-mode strand geometry is shown for clarity.

S3 Interpretation of twist-induced mode coupling as a grating effect

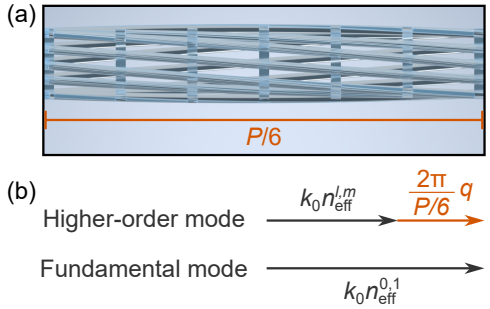

Fig S3 Interpretation of twisted waveguides as gratings. (a) Side view of a twisted light cage with 6-fold rotational symmetry. Its cross section repeats after a distance $P/6$, while each individual strand features a helical pitch distance P. (b) Wavevectors involved in coupling of two core modes. The grating vector of the twisted waveguide (orange) mediates the phase matching. Note that the spin- and OAM-selectivity is hidden in the order q, as the grating can only couple modes with $\Delta j = 6q$.

S4 Simulation results for additional twist-induced resonances

Here, two more resonances in twisted light cages are analyzed, completing the analysis presented in Fig. 3. The simulation results corroborate the explanation of twist-induced resonances in Sec. 3.

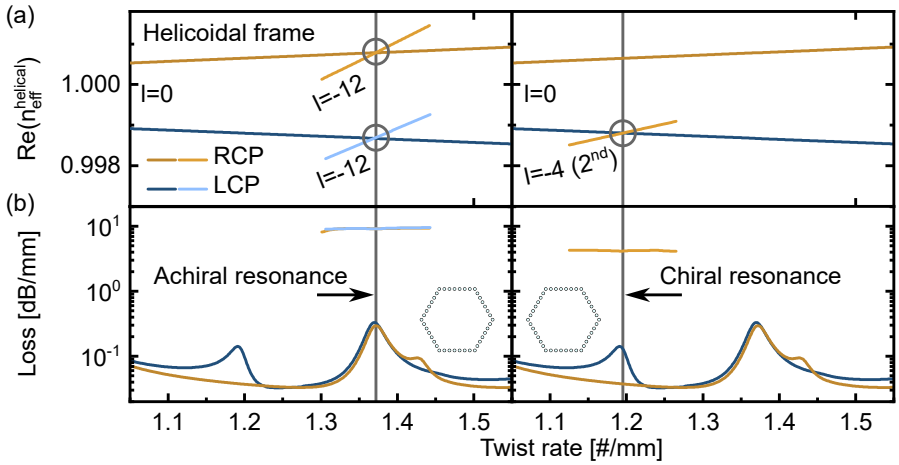

Fig S4 Further twist induced resonances in single-mode strand light cages supplementing Fig. 3. (a) Real part of the effective index in the helicoidal frame and (b) attenuation of the fundamental core modes ($l = 0$) and relevant higher-order core modes. Left panel shows the second achiral resonance ($\Delta s = 0,\ \Delta l = 12$), and right panel a further chiral resonance ($\Delta s = +2,\ \Delta l = 4$). The OAM mode involved in the chiral resonance is of second radial order (i.e., $m = 2$ in the notation used for the tube model in Sec. 6).

S5 Spiraling phase patterns in OAM modes

Fig. 3(c) shows that modes carrying OAM feature a spiraling phase profile on the outside of the core, which is different from the OAM phase profile inside the core. The spiraling pattern arises as the sum of an OAM phase profile with that of a diverging lens whose focal length is found to be largely independent of twist rate and OAM order. The diverging field outside of the core might be related to the higher propagation loss of OAM modes compared to the fundamental modes, as energy is constantly carried away from the core.

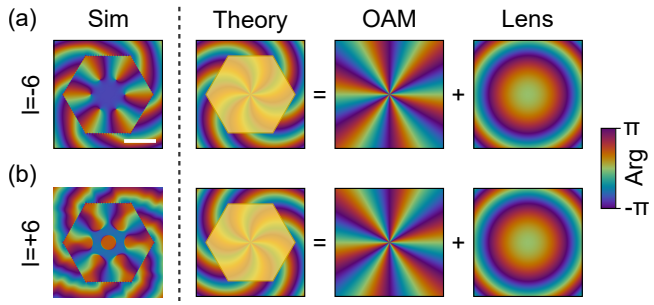

Fig S5 Interpretation of "spiraling" phase profile of OAM modes shown in Fig. 3. For negative OAM (a), the phase profile twists counterclockwise outside of the core region, while it twists clockwise for positive OAM (b). Phase profiles on the left were simulated for a RCP mode at a twist rate of 0.8/mm. The twisting phase profile can be modeled as the sum of an $\exp(\mathrm{i}l\phi)$ phase profile and the phase of a diverging lens (focal length: -190 µm). Inside the core (yellow shaded area), the phase profile does not twist. Scale bar denotes 10 µm.

S6 Refractive index of IP-Dip polymer

The dispersion of the polymerized resist, from which the waveguide is made, is provided by Nanoscribe GmbH in the form of a single-term Sellmeier equation (shown in Fig. S6):

$$n(\lambda) = \sqrt{1 + \frac{A_1 \lambda^2}{\lambda^2 - \lambda_1^2}}, \tag{S1}$$

with $A_1 = 1.3424689$ and $\lambda_1 = 0.128436$ µm. More detailed formulas including the imaginary part of the refractive index and its changes under different polymerization conditions can be found in Ref. [93]. In our analysis, we neglected the losses of the polymer because (1) only a negligible portion of the field is guided inside the polymer, and (2) scattering losses due to surface roughness of the polymer are likely higher than the intrinsic loss of the material.

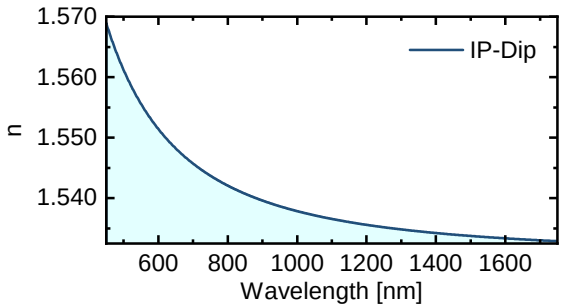

Fig S6 Refractive index of the polymerized resist (IP-Dip, Nanoscribe GmbH) calculated using Eq. (S1).

S7 Convergence of the FEM simulation

The convergence of the real and imaginary part of $n_{\text{eff}}^{\text{helical}}$ with decreasing mesh size in the core and strands of a multimode strand twisted light cage strand diameter of $D = 3.6$ µm is shown in Fig. S7. As evident from the insets in Fig. 5(d) the fundamental mode of the twisted light cage develops more and more fine features as the twist rate increases which requires the use of finer meshes. A mesh size that yields sufficient convergence for this geometry at all investigated twist rates was $\lambda/6$ in the strands and $\lambda/2$ in the core. For $\lambda = 770\ \text{nm}$ this results in a mesh consisting of 117,950 triangles.

If the eigenvalues do not converge with decreasing mesh size, the distance between the outermost part of the structure and the PML should be adjusted. If the distance is too small, unwanted interactions with the PML might occur. If the distance is too large, the solver might not be able to find the correct eigenmode.

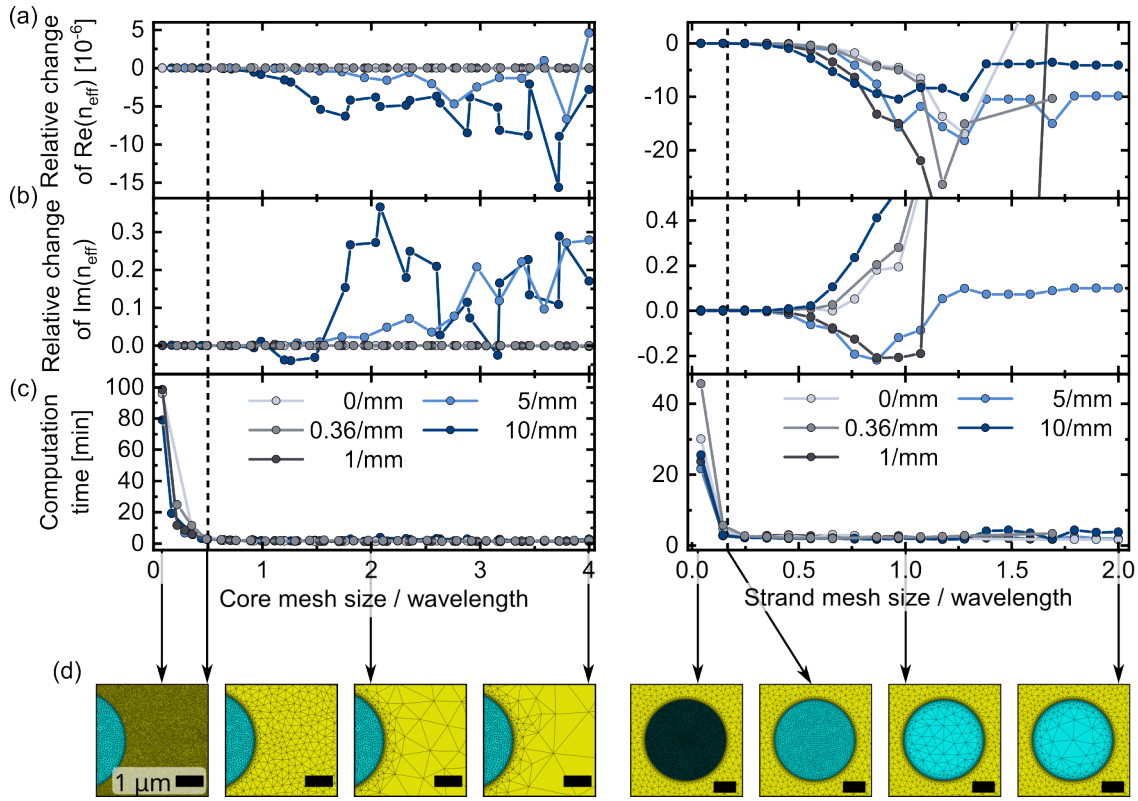

Fig S7 Convergence of the FEM simulation of the effective index $n_{\text{eff}}^{\text{helical}}$ with decreasing mesh size on the example of a twisted multimode-strand light cage. Convergence was checked for twist rates ranging from 0 to 10 twists per mm as indicated in the legend. The mesh size was varied both in the hollow core (left panels, yellow region) and in the strands (right panels, blue region). Real (a) and imaginary (b) part of $n_{\text{eff}}^{\text{helical}}$ have converged to a satisfactory level for all twist rates once the mesh size reaches $\lambda/2$ in the core and $\lambda/6$ in the strands (dashed black lines). For even smaller mesh sizes, the computation time increases strongly (c). Selected meshes for the sizes indicated by the arrows are depicted in (d). The RCP fundamental mode of the light cage was simulated at $\lambda = 770\ \text{nm}$. For the simulations in the left panels, the mesh size in the strands was fixed to $\lambda/6$, while the mesh size in the core was fixed to $\lambda/2$ in the right panels.

S8 Helicoidal coordinate frame

The helicoidal frame is a local coordinate system used to describe structures that are invariant under twisting (i.e., invariance under a combination of rotation and translation). Helicoidal coordinates

(ξ_1, ξ_2, ξ_3) are related to Cartesian coordinates (x, y, z) via [25]:

$$\mathbf{r} = \begin{pmatrix} x \\ y \\ z \end{pmatrix} = \begin{pmatrix} \xi_1 \cos(\alpha\xi_3) + \xi_2 \sin(\alpha\xi_3) \\ -\xi_1 \sin(\alpha\xi_3) + \xi_2 \cos(\alpha\xi_3) \\ \xi_3 \end{pmatrix} \quad \Leftrightarrow \quad \begin{pmatrix} \xi_1 \\ \xi_2 \\ \xi_3 \end{pmatrix} = \begin{pmatrix} x\cos(\alpha z) - y\sin(\alpha z) \\ x\sin(\alpha z) + y\cos(\alpha z) \\ z \end{pmatrix}. \tag{S2}$$

For fixed values ξ_1 and ξ_2, the curve $\mathbf{r}(\xi_3)$ is a left-handed helix for $\alpha > 0$. The basis vectors of the helicoidal frame are given by:

$$\begin{aligned} \boldsymbol{\xi_1} = \frac{\partial \mathbf{r}}{\partial \xi_1} &= \begin{pmatrix} \cos(\alpha\xi_3) \\ -\sin(\alpha\xi_3) \\ 0 \end{pmatrix}, \qquad \boldsymbol{\xi_2} = \frac{\partial \mathbf{r}}{\partial \xi_2} = \begin{pmatrix} \sin(\alpha\xi_3) \\ \cos(\alpha\xi_3) \\ 0 \end{pmatrix}, \\ \boldsymbol{\xi_3} = \frac{\partial \mathbf{r}}{\partial \xi_3} &= \begin{pmatrix} -\xi_1\alpha\sin(\alpha\xi_3) + \xi_2\alpha\cos(\alpha\xi_3) \\ -\xi_1\alpha\cos(\alpha\xi_3) - \xi_2\alpha\sin(\alpha\xi_3) \\ 1 \end{pmatrix}. \end{aligned} \tag{S3}$$

Note that $\boldsymbol{\xi_3}$ is not normalized and the system $(\boldsymbol{\xi_1}, \boldsymbol{\xi_2}, \boldsymbol{\xi_3})$ is not orthogonal. Since $\boldsymbol{\xi_1}$ and $\boldsymbol{\xi_2}$ always lie in the xy plane, the helicoidal coordinate system is especially useful if the wavefronts of the fundamental mode are perpendicular to the z axis, which is the case for twisted light cages and most other on-axis twisted waveguides. Further coordinate frames in which twisted waveguides become invariant are the Frenet-Serret frame and the Overfelt frame [41].

In this work, the invariance of twisted waveguides along the ξ_3 coordinate is used to perform the optical simulations in two dimensions reducing computation time compared to a full 3D simulation. This is possible because the vector wave equations (Eq. (S5)) have the same form in

any coordinate frame if the material properties ($\underline{\epsilon}$, $\underline{\mu}$) are replaced by modified material properties ($\underline{\epsilon}'$, $\underline{\mu}'$) [98]:

$$\underline{\epsilon}' = \underline{\mathbf{T}}^{-1}\underline{\epsilon}\,(\underline{\mathbf{T}}^{-1})^{\top}\det(\underline{\mathbf{T}}), \qquad \underline{\mu}' = \underline{\mathbf{T}}^{-1}\underline{\mu}\,(\underline{\mathbf{T}}^{-1})^{\top}\det(\underline{\mathbf{T}}), \tag{S4}$$

where $\underline{\mathbf{T}}^{-1}$ is the inverse of the Jacobian $\underline{\mathbf{T}} = (\xi_{\mathbf{1}}, \xi_{\mathbf{2}}, \xi_{\mathbf{3}})$ of the coordinate transformation, $^{\top}$ denotes the transposed matrix, and $\det$ the determinant. The vector wave equations of linear media used by the solver can be stated as [99]:

$$\begin{aligned} \boldsymbol{\nabla}\times\left(\underline{\mu_r}^{-1}\boldsymbol{\nabla}\times\mathbf{E}\right) + \frac{1}{c_0^2}\,\underline{\epsilon_r}\,\frac{\partial^2\mathbf{E}}{\partial t^2} &= 0, \\ \boldsymbol{\nabla}\times\left(\underline{\epsilon_r}^{-1}\boldsymbol{\nabla}\times\mathbf{H}\right) + \frac{1}{c_0^2}\,\underline{\mu_r}\,\frac{\partial^2\mathbf{H}}{\partial t^2} &= 0, \end{aligned} \tag{S5}$$

where c_0 is the speed of light in vacuum. As light cages are made from isotropic materials (i.e., material properties are scalars), Eq. (S4) reduces to [100]:

$$\underline{\epsilon}' = \epsilon\underline{\mathbf{G}}^{-1}, \quad \underline{\mu}' = \mu\underline{\mathbf{G}}^{-1}, \tag{S6a}$$

$$\text{with } \underline{\mathbf{G}}^{-1} = \left(\frac{\underline{\mathbf{T}}^{\top}\underline{\mathbf{T}}}{\det(\underline{\mathbf{T}})}\right)^{-1} = \begin{pmatrix} 1+\alpha^2\xi_2^2 & -\alpha^2\xi_1\xi_2 & -\alpha\xi_2 \\ -\alpha^2\xi_1\xi_2 & 1+\alpha^2\xi_1^2 & \alpha\xi_1 \\ -\alpha\xi_2 & \alpha\xi_1 & 1 \end{pmatrix}. \tag{S6b}$$

Twisting a waveguide therefore effectively results in the material properties becoming anisotropic, with the degree of anisotropy increasing with twist rate and distance from the twist axis. Furthermore, it is important to note that the curl operator in the vector wave equations takes on a nontrivial form as the helicoidal coordinate frame is not orthogonal [92].

Note, that the transformation of the material properties explained here is automatically carried

out by the used FEM solver (JCMwave).

S9 Transformation of the effective index to the lab frame

After transforming the effective index to the lab frame using Eq. (8), the index of the fundamental modes does not intersect anymore with those of the higher-order modes. This emphasizes that the angular momentum harmonics (which are neglected when applying Eq. (8)) are responsible for the twist-induced mode coupling.

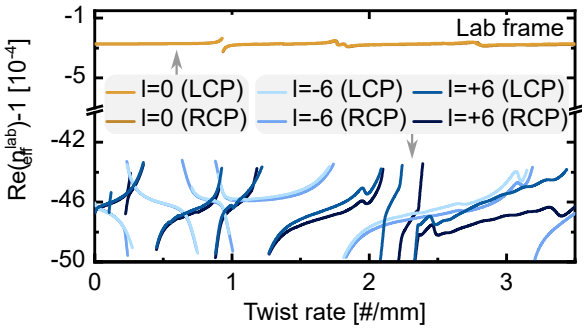

Fig S8 Real part of the effective index of fundamental and higher-order modes with $|l| = 6$ in the lab frame. Results were calculated for a twisted single-mode strand light cage. The corresponding figure showing the results in the helicodal frame are shown in Fig. 3(a).

S10 OAM decomposition

An example of an OAM decomposition of the fundamental RCP mode (i.e., $j_0 = -1$) of an untwisted light cage is shown in Fig. S9 below. In this example, only the x component of the electric field was analyzed. The resulting OAM distribution therefore contains peaks at $l = 6q$ and $l = 6q - 2$ corresponding to the two different spin contributions.

To determine the spin state of the OAM harmonics identified in Fig. S9, the modes are first decomposed into the two spin states (as described in Sec. 10.4), such that the OAM decomposition can be carried out separately for each spin state. The results of this analysis are shown in Fig. S10, which is a more detailed version of Fig. 4(e) of the main text.

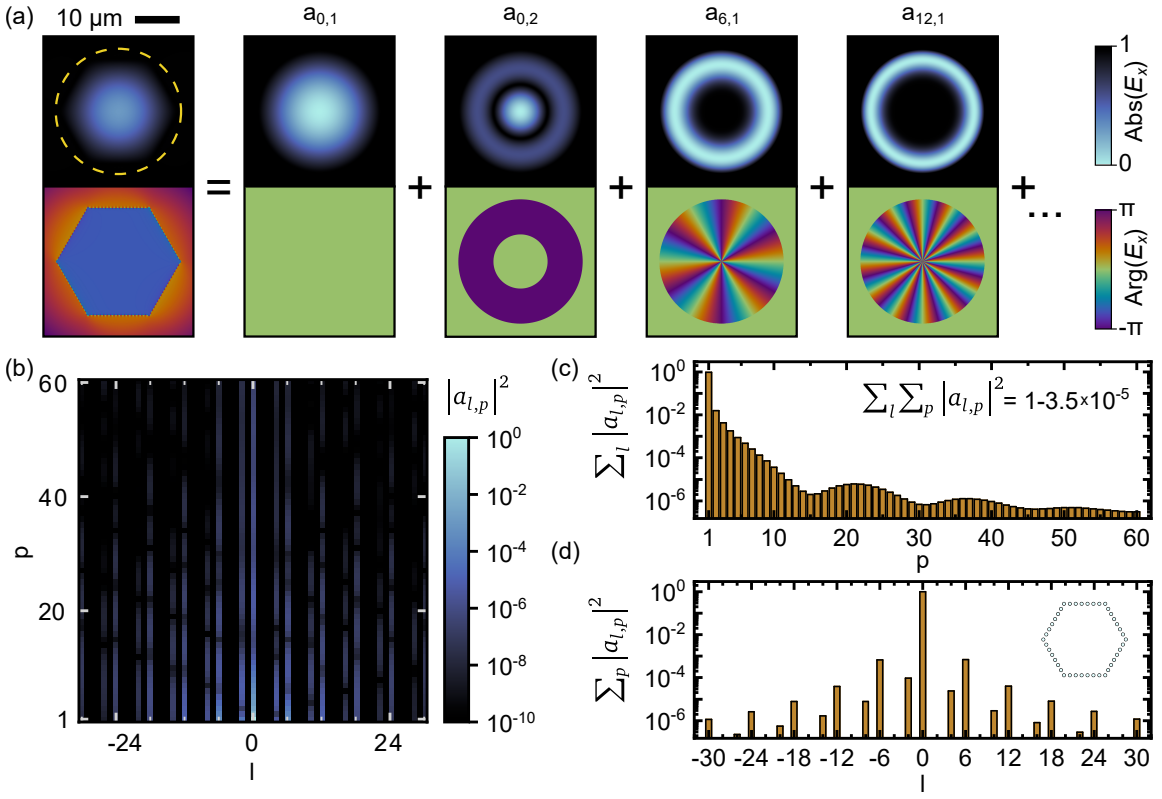

Fig S9 Decomposition of a mode into Bessel beams for analyzing its OAM content. (a) The electric field E_x of the RCP fundamental mode of an untwisted single-mode strand light cage (left panel) can be decomposed into a series of Bessel beams Ψ_{lp} with amplitudes $a_{l,p}$ according to Eq. (10) (right panels). Ψ_{lp} is defined within a circle of radius R_0 (yellow dashed line) with values on the boundary being 0. Field values outside of this circle are not analyzed. (b) Distribution of $|a_{l,p}|^2$ up to $|l| = 30$ and $p = 60$ for the mode shown in (a). (c,d) Summing $|a_{l,p}|^2$ over l or p shows the convergence of the decomposition procedure. The sum over all squared amplitudes is close to 1 indicating a good fit (c).

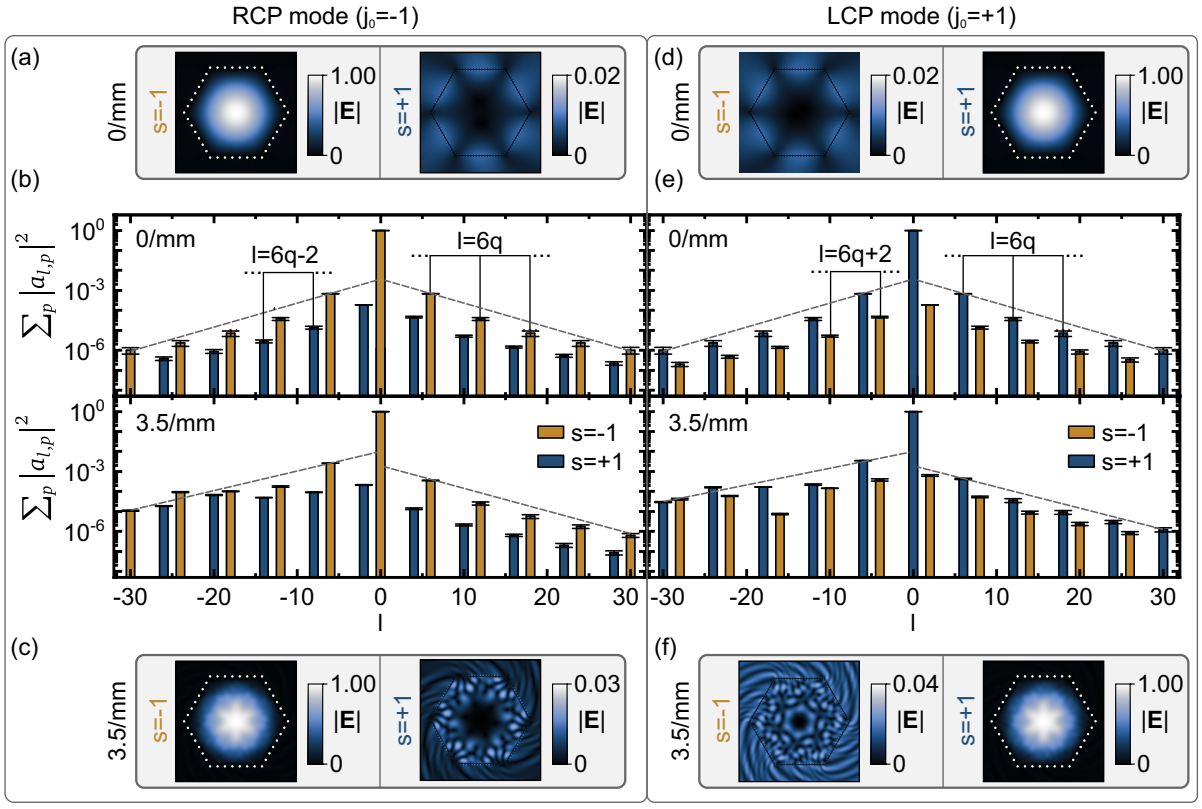

Fig S10 OAM decomposition of RCP (left panels) and LCP fundamental mode (right panels) of a single-mode strand light cage at twist rates of 0/mm (top) and 3.5/mm (bottom). (a,c) Magnitude of the electric field of the two spin contributions of the RCP mode in the untwisted waveguide. Twist rates are indicated on the left. As expected, the mode predominantly carries the $s = -1$ spin state. Blue dots show the simplified geometry (for the dominant spin state only). (b) OAM decomposition carried out separately for each of the spin contributions at the twist rates indicated in the panels. The dominant spin contribution ($s = -1$) features OAM harmonics of the form $l = 6q$, while the weaker spin contribution ($s = +1$) causes peaks at $l = 6q - 2$. As expected, the total angular momentum of all contributions is equal to $j = -1 + 6q$. Gray dashed lines are a guide to the eye indicating that the amplitudes of the negative OAM harmonics increase with twist rate. The horizontal lines on top of the bars are an estimate of the error of the OMA decomposition as described in Sec. 10.4. (d,e,f) Analogous to (a,b,c) for the LCP mode.

S11 Comparison between hexagonal and round arrangement of the strands

To demonstrate the effect of the waveguide geometry on the optical properties of the twisted waveguide, additional simulations were performed for a single-mode strand light cage with a circular arrangement of the 108 strands. As shown in Fig. S11, the RCP fundamental mode in the round variant features OAM harmonics with $l = 108$ and $l = 108 - 2$, as expected.

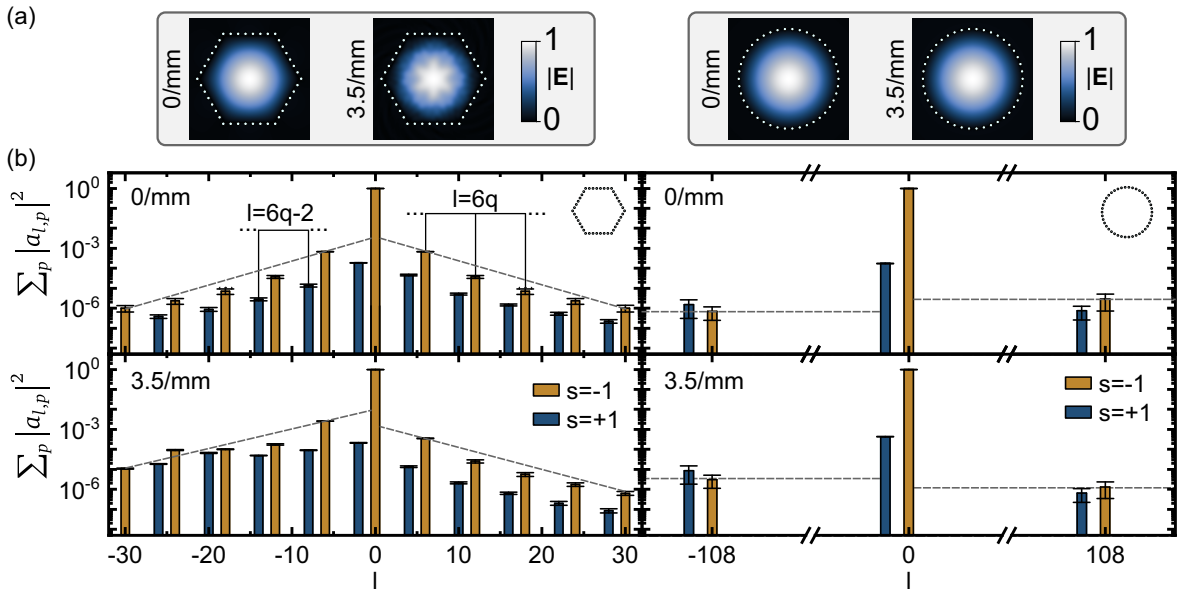

Fig S11 Comparison of OAM decomposition between hexagonal (left panels) and round (right panels) single-mode strand light cages on the example of the RCP fundamental mode. (a) Magnitude of the electric field at the indicated twist rates. Both geometries consist of 108 strands and are shown in a simplified versions as blue dots. (b) OAM decomposition indicating dominant RCP (orange) and weak LCP (blue) components of the RCP mode. Twisting shifts the average of the OAM distribution towards negative values for a left-handed twist (lower panels in b, gray dashed lines are a guide to the eye). The horizontal lines on top of the bars are an estimate of the error of the OMA decomposition as described in Sec. 10.4.

The reduced number of OAM harmonics in the round arrangement leads to a reduction in the number of allowed twist-induced resonances, as predicted by Eq. (2). The corresponding simulation results are shown in Fig. S12.

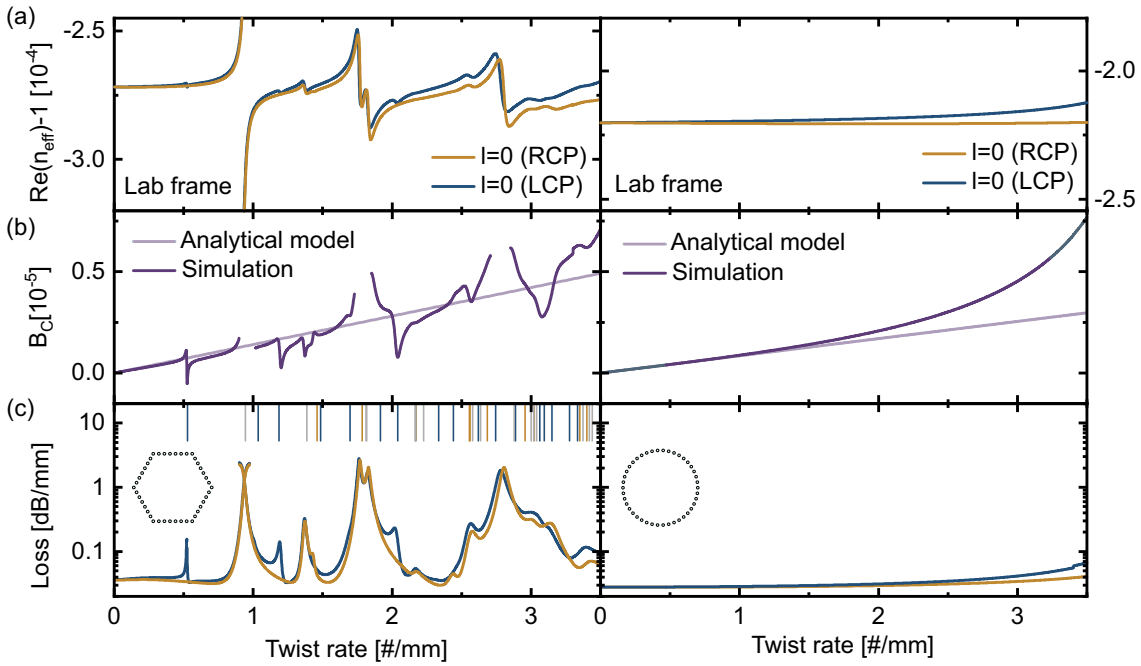

Fig S12 Comparison of optical properties of twisted single-mode strand light cages in the lab frame. Left panels show the hexagonal, right panels the round geometry. (a) Real part of the effective index of the RCP and LCP fundamental mode. (b) Circular birefringence. Light purple line is an analytical prediction based on the properties of the untwisted waveguide (Eq. (4)). (c) Attenuation of the fundamental core modes. Vertical lines are predictions for the resonances according to Eq. (S9) (blue: LCP, orange: RCP, gray: LCP and RCP). Insets in (c) depict the simplified geometries.

S12 Tube waveguide model

Here we show that untwisted light cages can be approximated as a tube to obtain an analytic expression for the effective indices of the higher-order modes based on the dispersion of the fundamental mode. To this end, we apply a recently reported model for tube-type hollow-core fibers [47], with the geometry shown in Fig. S13.

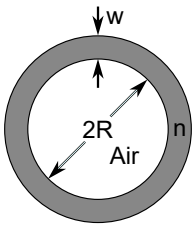

Fig S13 Geometry of the tube waveguide model of Ref. [47]. The model applies to waveguides where the cross section is a ring with inner radius R, thickness w, and refractive index n.

The model approximates the cladding surface to be locally flat, which is a good approximation

for the large core radii of light cages ($R \gg \lambda$). If the core is filled with air, the effective index of its modes can be described as [47]:

$$n_{\mathrm{eff}}^{l,m} = 1 - \frac{u_{l,m}^2}{2}(k_0 R)^{-2} - \frac{u_{l,m}^2}{2}\frac{n^2+1}{\sqrt{n^2-1}}(k_0 R)^{-3}\cot\left(k_0 w\sqrt{n^2-1}\right) + \mathcal{O}\left((k_0 R)^{-4}\right), \quad \text{(S7)}$$

where $u_{l,m}$ is the m^{th} root of the l^{th} order Bessel function of the first kind. $l = ..., -1, 0, 1, ...$ and $m = 1, 2, ...$ refer to the azimuthal and radial order of the modes, respectively, akin to the definition of LP modes. HE and EH vector modes are grouped together in this equation by neglecting contributions of $\mathcal{O}\left((k_0 R)^4\right)$. The equation also holds for TE and TM modes if the refractive index contrast is low ($n \approx 1$). Since the following analysis is based on modes with $|l| \neq 1$, TE and TM modes can be neglected entirely.

The model is verified using the fundamental modes of the multimode and single-mode strand light cage. As shown in Fig. S14, the model is in good agreement with the simulated effective index with small deviations occurring around the resonances.

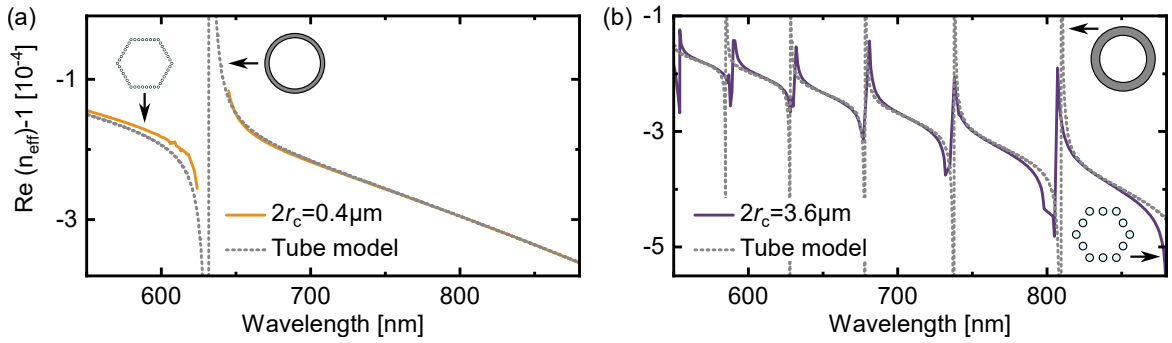

Fig S14 Application of the tube waveguide model of Ref. [47] to light cages. The model (gray dotted line) accurately describes the dispersion of untwisted light cages with single-mode strands of diameter $2r_c$ of 0.4 µm (a) and multimode strands of diameter 3.6 µm (b). The fitted parameters were: $R = 12.37$ µm; $w = 0.267$ µm for (a), and $R = 11.5$ µm; $w = 3.448$ µm for (b).

The fitted parameters R and w are remarkably close to the hexagon radius $\rho = 14$ µm and strand diameter $2r_c$ of the light cage, showing that the strand supermodes of the light cage indeed

behave like a tube that confines the light inside the core.

Having determined the parameters of the model, Eq. (S7) can be used to estimate the index of all higher-order modes, which only depends on $u_{l,m}$ for a fixed wavelength:

$$n_{\text{eff}}^{l,m} \approx 1 - A\, u_{l,m}^2, \tag{S8}$$

where $A(\lambda)$ does not depend on the order of the mode. The quadratic dependence of the indices on $u_{l,m}$ matches well with the simulated modal indices as shown in Fig. S15. Plugging this relation into Eq. (2) then allows to determine the twist rates at which resonances may occur:

$$\alpha\, \Delta j \approx A\, k_0 (u_{\tilde{l},\tilde{m}}^2 - u_{0,1}^2). \tag{S9}$$

Note that for large values of l or m, the function $u_{l,m}$ grows approximately linearly in m and l.

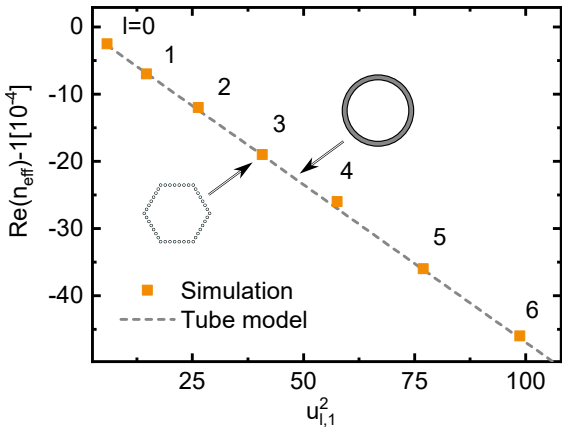

Fig S15 Effective index of higher-order modes in untwisted single-mode strand light cages. Indices of modes of radial order $m = 1$ and azimuthal orders l ranging from 0 to 6 were simulated (orange squares). Gray dashed line corresponds to the tube model (Eq. (S8)) with parameters obtained from the dispersion of the fundamental mode ($m = 1, l = 0$).

S13 Simulaton results for multimode strand light cages

The analysis of multimode strand light cages in the main part of the paper was limited to the four twist rates of the fabricated samples. Here, additional results are presented for intermediate twist rates. Note that these results were calculated for a strand diameter of $2r_c = 3.6$ µm with left-handed twisting direction, while the results shown in Fig. 5 pertain to right-handed structures with $2r_c = 3.814$ µm.

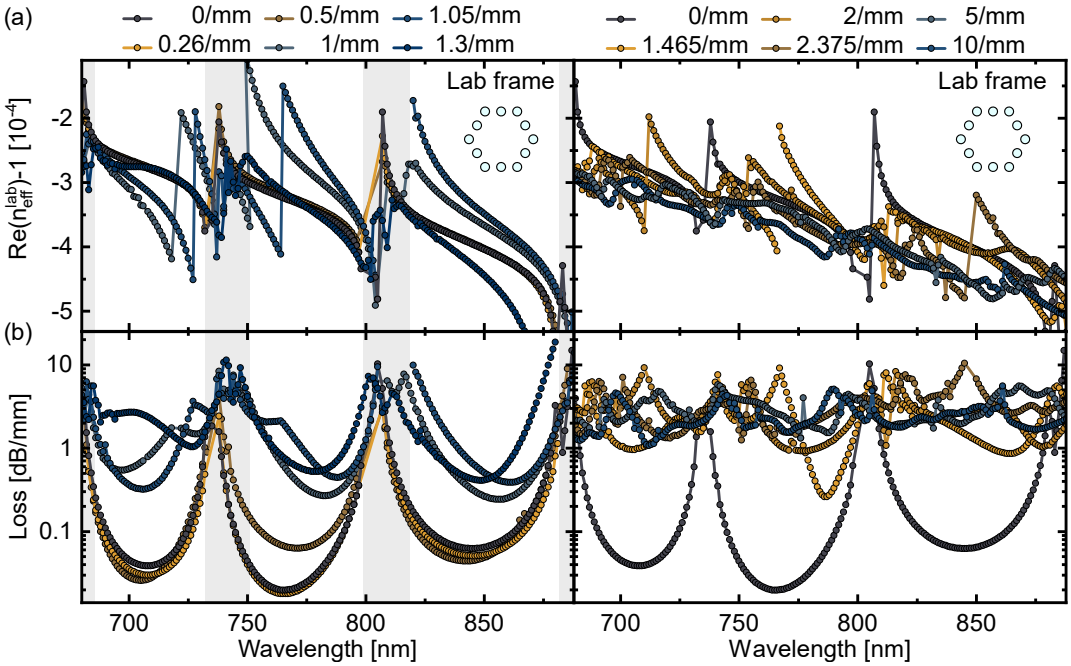

Fig S16 Dispersion (a) and attenuation (b) of the RCP fundamental mode in multimode strand light cages at different twist rates. Dispersion was calculated in the lab frame using Eq. (8). Left panel: low twist rates (0 - 1.3/mm). Right panel: high twist rates (1.465 - 10/mm). Twisting induces resonances to higher-order core modes, e.g., at a wavelength of 770 nm for a twist rate of 1.05/mm.

The left panel of Fig. S16 and Fig. S17 indicate that the spectral position of core-strand resonances is nearly unaffected by twisting. This can be understood based on the analysis of off-axis twisted waveguides in [41]. The strands of multimode strand twisted light cages correspond exactly to the multimode helicoidal waveguides analyzed in this reference. Twisting was shown to increase the effective modal index of the strands due to the increased path that the light has to

travel along the helical trajectory. However, light in the hollow core remains on the twist axis and is therefore not forced to travel along an elongated path. Thus, the effective index of the core mode (evaluated in the lab frame) does not increase with twist rate as shown in Fig. S8. Since the index of the core is lower than that of the strands, twisting only increases this index difference further. Core-strand resonances therefore still only occur at the cut-offs of the strand modes, which are apparently unaffected by twisting.

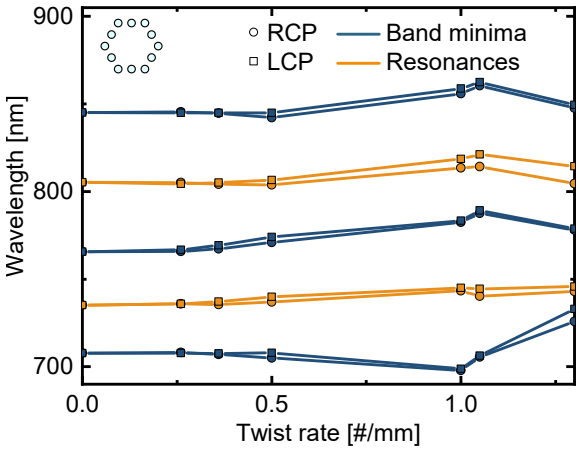

Fig S17 Impact of twisting on the spectral position of core-strand resonances and transmission band minima. Analysis was performed for multimode strand light cages based on the data in Fig. S16. Positions of core-strand resonances (orange) remain mostly unaffected by twisting while transmission band minima (blue) may shift due to twist-induced core-core resonances.

S14 Increased loss at high twist rates

Both, in the experimental and the simulation results shown in Fig. 5 the average propagation loss increases at high twist rates. One possible explanation is that with an increased twist rate, the core mode couples to more and more lossy higher-order core modes, thus increasing the propagation loss. To estimate the number of resonances occurring within the observed wavelength range, we use the tube waveguide model reported in Sec. S12. As expected, the results shown in Fig. S18 indicate an increase in the number of resonances with twist rate, making this a likely explanation for the observed increase in propagation loss.

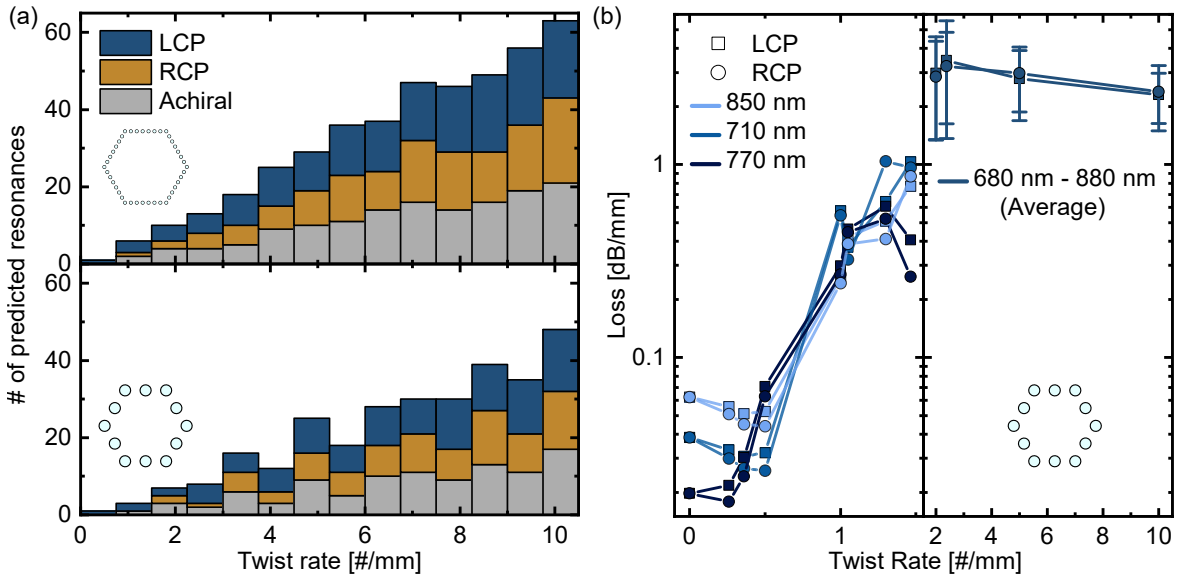

Fig S18 Explanation for increased loss at high twist rates. (a) The number of allowed resonances (chiral: blue/orange, achiral: gray) increases with twist rate according to Eq. (S9) both for the single-mode strand (top) and multimode strand variant (bottom). (b) The attenuation of the fundamental modes in the multimode strand light cage increases strongly with twist rate. For low twist rates (left side), the loss was evaluated at the off-resonance point of the three transmission bands indicated in the legend (data was taken from Fig. S16). For high twist rates, individual transmission bands cannot be distinguished and the loss was averaged between 680 nm - 880 nm (right side). Error bars denote the corresponding standard deviation.

S15 Optical measurement setup

The setup shown in Fig. S19 was used for the measurement of circularly polarized light through the waveguides. All components and the measurement procedure are described in Sec. 10.6.

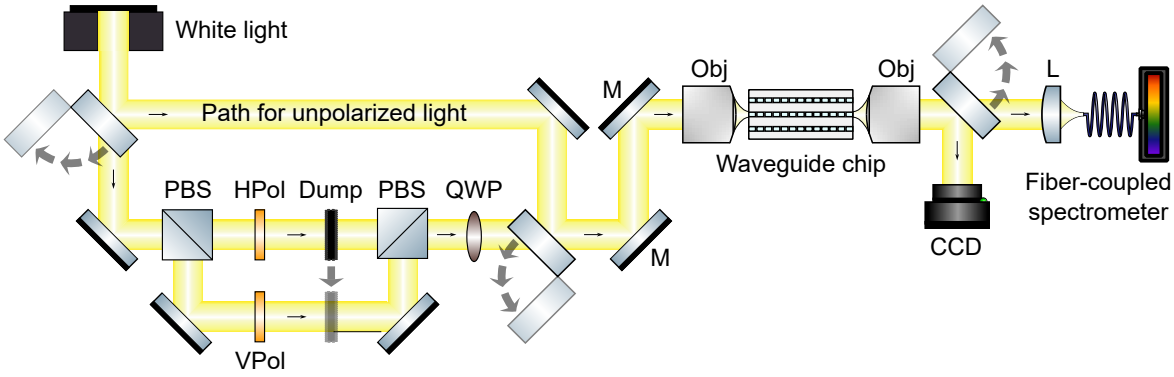

Fig S19 Setup for transmission and circular dichroism measurements. White light: supercontinuum laser source, PBS: polarizing beamsplitter, HPol/VPol: horizontal/vertical linear polarizer, QWP: quarter waveplate, Qbj: objective, CCD: camera, L: lens, M: mirror pair for beam steering. Flip mirrors determine whether polarized or unpolarized light is sent to the waveguide chip, and a beam dump is used for selecting a specific polarization. Component library from Ref. [97] was used to create this figure.

The setup allows light of several polarization states to be used, in particular unpolarized, linearly polarized (horizontal/vertical with respect to the plane of the sample substrate), and circularly polarized (LCP/RPC) light. For the circular dichroism measurements, circularly polarized light is generated by two linear polarizers and a quarter waveplate with its optical axis oriented at a 45° angle with respect to the axis of the polarizers.

Measurements with circularly polarized light pose additional requirements on the setup because reflections and refractions on any surface reduce the degree of circularity of the polarization state, thus creating elliptically polarized light (because the Fresnel reflection coefficients are generally different for TE and TM incidence [96]). To avoid this, the quarter waveplate is the last optical element before the light is coupled to the waveguide.

Furthermore, any shifts of the beam need to be avoided when switching between LCP and RCP light as such shifts would change the amount of light that is coupled to the waveguide, thus leading to false positive CD measurements. To avoid any mechanical movement, the two linear polarizers are placed in the arms of a Mach Zehnder interferometer beam path. By blocking one arm of the beam path, a specific linear polarization (horizontal or vertical) is selected, which translates to a specific circular polarization after the quarter waveplate. The beam path is created using two polarizing beamsplitters (Thorlabs PBS252, 620 - 1000 nm) to avoid the 75% loss that would occur for non-polarizing beamsplitters. For accurate measurements, a precise overlap of the two beams created in the interferometer is essential, which is achieved by ensuring that the beam positions match at two points that are about 1.5 m apart: an iris at the output of the interferometer and the pinhole represented by the multimode fiber.

S16 Impact of support elements on the propagation loss

While support rings and support blocks cannot be included in the simulations because they break the translational invariance of the waveguide, we argue that their impact on the propagation loss is limited by calculating the fraction of optical power, η, that is confined within the hexagonal core (and thus not present in the region of the support elements). Specifically, η is determined by integrating the z component of the Poynting vector over the hexagonal core and comparing it to the integral over the entire simulation domain. It should be noted that the simulation area was limited to the immediate vicinity of the light cage cross section since the radiation caustics (i.e. the point at which the field changes its character from decaying to rising [101]) is far away from the light cage surface and can therefore be neglected (cf. Supporting Information of Ref. [34]). This resulting fraction η is $> 99.5\ \%$ for both untwisted and highly twisted light cages at a wavelength of 770 nm (Fig. S20). Therefore, it can be concluded that the loss caused by the support elements is negligible.

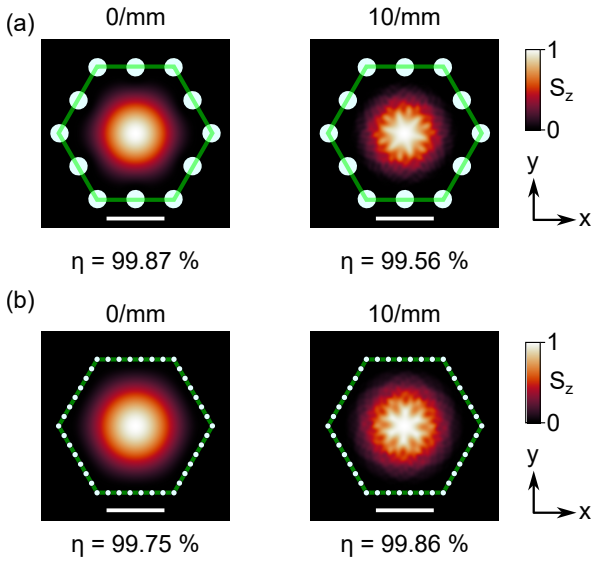

Fig S20 Fraction of optical power η guided inside the hexagonal core in the untwisted and strongly twisted case. (a) Multimode strand light cage (b) Single-mode strand light cage. Core area is highlighted by the green line. Simulations were performed at $\lambda = 770$ nm. Scale bar denotes 10 µm.

S17 Comparison between hexagonal and triangular arrangement of the strands and the impact of core size

To further investigate the influence of rotational symmetry on the twist-induced resonances, additional simulations were performed for a triangular arrangement of the single-mode strands (C_{3z} symmetry). The dimensions of the waveguide were chosen such that it has the same circumference radius (14 µm) and strand-to-strand spacing Λ as the hexagonal counterpart, resulting in a total number of 93 strands instead of the 108 in the hexagonal variant.

This choice of parameters leads to a reduced mode area in the triangular geometry, as evident from the lower effective index in the untwisted waveguide (Fig. S21(a)). Therefore, the effective index spacing between the fundamental and OAM modes is larger in the triangular configuration than in the hexagonal one, consistent with the predictions of the tube waveguide model (Eq. (S7)). As a result, the number of twist-induced resonances within the studied twist rate range is reduced in the triangular variant (Eq. (2)), despite the angular momentum selection rule permitting a greater number of OAM modes to be excited by the fundamental modes (Eq. (3)).

In contrast to the circular arrangement of the strands, the triangular configuration exhibits a higher circular birefringence than the hexagonal variant (Fig. S21(b)). This increase occurs because the rotational invariance of the modes is broken to a greater extent by both the triangular geometry and the smaller core size (see Eq. (4)).

It should also be noted that the propagation loss in untwisted antiresonant waveguides is known to scale approximately inversely with the fourth power of the mode diameter [47]. Thus, the reduced mode area in the triangular arrangement leads to an overall higher propagation loss (Fig. S21(c)).

In summary, a smaller core size results in (i) increased circular birefringence, (ii) fewer resonances per twist rate interval, and (iii) overall higher propagation loss.

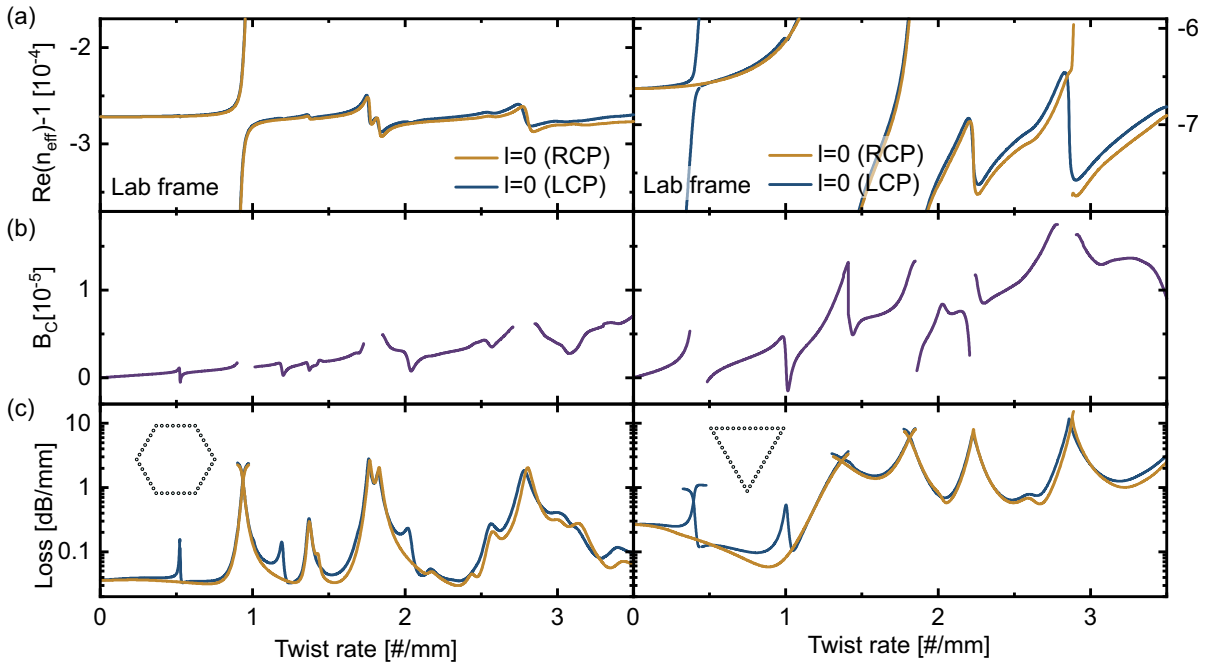

Fig S21 Comparison of optical properties of two types of twisted single-mode strand light cages in the lab frame. Left panels show the hexagonal, right panels a triangular geometry. (a) Real part of the effective index of the RCP and LCP fundamental mode. (b) Circular birefringence. (c) Attenuation of the fundamental core modes. Insets in (c) depict simplified geometries with a reduced number of strands.